Linking Ab initio density functional theory with modelling reaction microkinetics to understand catalytic fatty acids hydro-deoxygenation intermediate species selectivity

Matej Žula [a,b,f], Žan Kovačič [a], Vid Bačar [a,e], Michal Mazur [g], Matej Huš [a,h,i], Blaž Likozar [a,c,d,e,*]

[a] Department of Catalysis and Chemical Reaction Engineering, National Institute of Chemistry, Hajdrihova 19, SI-1001 Ljubljana, Slovenia
[b] University of Nova Gorica, Vipavska 13, SI-5000 Nova Gorica, Slovenia
[c] Pulp and Paper Institute, Bogišićeva 8, 1000 Ljubljana, Slovenia
[d] Faculty of Polymer Technology, Ozare 19, SI-2380 Slovenj Gradec, Slovenia
[e] Faculty of Chemistry and Chemical Technology, University of Ljubljana, Večna pot 113, SI-1000 Ljubljana, Slovenia
[f] Department of Chemistry, Technical University of Munich, Lichtenbergstraße 4, 85748, Garching, Germany
[g] Department of Physical and Macromolecular Chemistry, Faculty of Science, Charles University, Hlavova 8, 128 43 Prague 2, Czech Republic
[h] Association for Technical Culture of Slovenia, Zaloška 65, SI-1000 Ljubljana, Slovenia
[i] Institute for the Protection of Cultural Heritage of Slovenia, Poljanska 40, SI-1000 Ljubljana, Slovenia

ABSTRACT

Catalyst surfaces enable the catalytic reactions via binding of substrates and lowering the reaction barriers to obtain the desired products. Separating the binding process from the reaction barriers enables us the understanding of surface properties and enables the reaction engineering strategies such as choice of solvents or functional groups protections. Through the modelling of the hydrodeoxygenation (HDO) of fatty acids, namely Stearic, Oleic, Linoleic, Myristic and Decanoic acid we show why the alkanes are the ideal solvent choice for NiMoS catalyst, why the alcohols side products form, regardless of the kinetic constant indicating fast dehydration, why the aldehydes intermediates are rarely detected and why hydrogenation of double bonds supersedes other kinetics events. We confirm the DFT calculations by integrating them into the kinetic model which confirms that the obtained results are sensible and usable in reaction engineering. The results are supported by the detailed characterization of the NiMoS catalyst.

1. Introduction

The defunctionalisation reactions are a crucial step in preparing the feedstocks for refining [1]. Removal of heteroatoms, namely oxygen, nitrogen, and sulphur, prevents the poisoning of acidic and metal sites in subsequent refining steps and enables stable preparation of fuels. The defunctionalisation has thus a long tradition in the Oil and Gas industry. However, with the development of renewable fuels the need for technology transfer occurred, new feedstocks are usually richer in oxygen and depending on the source, nitrogen, while containing less sulphur [2]. With the renewable diesel and SAF (sustainable aviation fuels) demands rising and supply unable to satisfy demand there is a high potential reward for being able to expand the number of feedstocks to those high in oxygen and nitrogen [3,4]. These species include novel functionalities which then compete for the active sites on the catalyst, by covering them, possibly to the level of poisoning them [5,6] or on the

other hand not being able to establish sufficient coverage due to lower affinity otherwise known as a lower binding energy barrier.

Experimental method to estimate these affinities usually includes reacting these functionalities separately and in combination with each other per example by deoxygenating palmitic acid and hexadecanol over NiMoS catalyst, together and separately and observing the change in the reaction rate it is easily noticeable that hexadecanol will be dehydrated about 10 times faster when palmitic acid is not present. However, with an increasing number of functionalities with different chain lengths the number of required experiments increases exponentially. Additionally, the situation becomes even more complicated with other functionalities or poisons that appear in traces or can be rapidly transformed at full coverage such as double bonds [5–7].

The density functional theory (DFT), offers sufficient prediction of all energy barriers for the systems including smaller molecules such as ammonia synthesis [8], CO_2 reduction [9], propane dehydrogenation

---

* Corresponding author.
  E-mail address: blaz.likozar@ki.si (B. Likozar).

[10] and more. However, computation time increases significantly when the molecules size reaches C_{16} or even higher and the computational chemistry can often be discarded by experimentalists that deal with such problems. In the article we show the relatively simple use of extrapolation of the DFT data that could be used to determine the coverages, based on the different functionalities significantly decreasing the need for the experimentation.

The commercial catalysts for preparation of feedstocks largely include supported and non-supported sulfided Ni- and Co-MoS catalysts [3,11–14]. Their robustness enables relatively stable application for most feedstocks while their price enables accessibility. It is thus reasonable to assume the continuous use of such catalysts for the defunctionalisation reactions and the necessary adaptation of the feedstocks might be easier and more cost-effective than the catalyst adaptation.

While the renewable fuels can be produced with little understanding of the mechanisms behind it, the understanding should improve the user experience, explain the observed events, and perhaps offer some ideas for the continuous improvements of the catalysts. While the kinetic descriptions of hydrodeoxygenations are relatively complex to model due to constant change in functionalities there were multiple mechanistic and kinetic descriptions of the process. The simplest model would include 0 order reactions rates [15]. Further the descriptions would be upgraded to the Langmuir Hinshelwood reaction kinetics [16–19] where the fatty acid concentration would determine the process reaction rates.

In the paper we present the kinetic model built on DFT obtained adsorption barriers. The kinetic model includes adsorption of all present species including the reaction species, solvent, carbon oxides and water. The impact of the homogeneous esterification reactions on the process is shown. The model includes a simplification of a single rate determining active site, which might be supported by the secondary active sites, such as acidic Al_2O_3 sites or stranded Ni sites. Beyond that state-of-the-art STEM analysis was applied to image the sample and to collect EDS elemental composition maps to analytically show the degree of sulfidation of Mo and Ni species.

2. Experimental

2.1. Materials

Stearic acid (Acros Organics,>97 %), octadecanol (Sigma Aldrich,>95 %), oleic acid (Penta Chemicals Unlimited, >97 %), linoleic acid (>97 %, TCI), octadecanal (Abcr, >95 %), octadecane (Sigma Aldrich, >99 %), heptadecane (Sigma Aldrich, >99 %), stearyl stearate (Sigma Aldrich, >99 %), myristic acid (TCI, >99 %), tetradecanol (Fluka, >97 %), tetradecanal (>96 %), tetradecane (TCI, >99.5 %), tridecane (Sigma Aldrich, >99 %), myristyl myristate (Biosynth, >95 %), decanoic acid (TCI, >98 %), decanol (TCI, >98 %), decanal (TCI, >97 %), decane (TCI, >99.5 %), nonane (TCI, >99,5%), decyl decanoate (TCI, >95 %), dodecane (TCI, >99 %), isopropanol (Honeywell, >99.8 %), dimethyl disulfide (DMDS) (Sigma-Aldrich, >99 %), NiMo/Al₂O₃, hydrogen (Messser, 5.0), Nitrogen (Messer, 5.0).

2.2. Experimental work

The experimental work was done in 75 mL Parr series 5000 Multiple Reactor system. Unless specified differently an equivalent of 0.1 mol L^{-1} fatty acid mixture in 30 g of dodecane and 0.25 g of freshly sulfided catalyst was used in the experiments. The reactor was sealed and N_2 was used to physically remove O_2 prior to pressurization with H_2 gas. The initial H_2 pressure was 50 bar, with the temperature range between 225 and 275 °C. Due to high melting point of Stearic acid heating tape was used on the sampling line. The samples were diluted with 1-propanol and filtered post dilution to avoid precipitation. The samples were then analysed with gas chromatography (GCMS–QP 2010 Ultra, Shimadzu, Kyoto, Japan) equipped with a nonpolar column (Zebron

ZB–5MSi, length 60 m, diameter 0.25 mm, film thickness 0.25 μm). MS (mass spectrometry) was used to identify the compounds while the concentrations were determined using FID (flame ionization detector). The GC method included the heat-up to 320 °C and where it was held for 20 min. Fatty acids peak tailing was neglected. FID response of alkenes was assumed to be the same as the one from the alkanes with the same chain length. The experimental errors were estimated through repetition of the experiment and applied as the relative errors.

2.3. Catalyst properties, characterization, and activation

Commercially available NiMo/Al₂O₃ catalyst was activated by sulfidation, detailed description can be found in our previous work [20].

The catalyst was previously characterized in the work of Grilc and Likozar [21] and our previous work [20].

Catalyst was additionally characterized using XRD, STEM and STEM-EDS elemental analysis. X-ray diffraction (XRD) patterns were characterized using PW3040/60 X'Pert PRO MPD diffractometer at 35 kV and 45 mA with Cu Kα radiation source (λ = 0.154 nm) in the 2θ range from 10° to 80° and using JCPDS database for reference.

2.4. STEM

Scanning transmission electron microscopy (STEM) measurements were performed using a JEOL JEM NEOARM-200F microscope equipped with Schottky type field-emission gun operating at 200 kV. Samples were prepared by direct deposition of the powder on copper holey carbon TEM grids (EMS, USA). Images were collected in scanning mode using a JEOL annular dark-field (ADF) and bright-field (ABF) detectors. Energy dispersive X-ray spectroscopy (EDS) element distribution maps were acquired using a JEOL JED-2300 energy dispersive X-ray analyzer.

Obtained data was used to estimate the degree of Ni and Mo sulfidation and the degree of NiMo alloying on the catalyst. We analysed the elementary composition data and extracted the overlap between the elements using numpy package in Python. We translated the pixels from the.bmp STEM-EDS images into Python data using module OpenCV2. The STEM image was divided into a 2D grid in which each pixel had its own coordinates and RGB based value. Since the background was black an algorithm in Eq. (1) (example for coverage of sulphur on molybdenum) was used to determine the coverage. Based on the data comparison between the individual elements, we determined the overlap between these elements. Additionally, we compared the more scarcely populated STEM-EDS figure areas to separate the effects of figure resolution.

$$Coverage = \frac{n(S \times \text{Mo} > 0)}{n(Mo)} \tag{1}$$

2.5. DFT calculations

Density functional theory (DFT) calculations were performed with the GPAW-21–6-0 package [22]. The PBE functional with PAW pseudopotentials were utilized. The energy cut-off was set at 450 eV, which was decided based on convergence results. Long range dispersion forces were accounted for using the Grimme D3 correction [23]. Spin polarization was not considered since magnetic moments were shown to be quenched.

The MoS₂ slab was built with 6x6 unit cell with 3-layer slab thickness. Only the middle layer was left, and the rest deleted, which was shown by previous report to reproduce experimental results of the studied catalyst very well [24,25]. On the surface 2 neighbouring atoms of Mo were substituted by Ni atoms (Figure S3). The report by Sun et al. [26] demonstrated that the substitution of Mo with Ni atoms is justified, where similarly to us they studied adsorption configurations. A 12 Å vacuum was added to avoid spurious inter-cell interactions. Additionally, a dipole correction [27] was applied in the z-direction. The supercells were probed by Monkhorst-Pack mesh [28], at gamma point
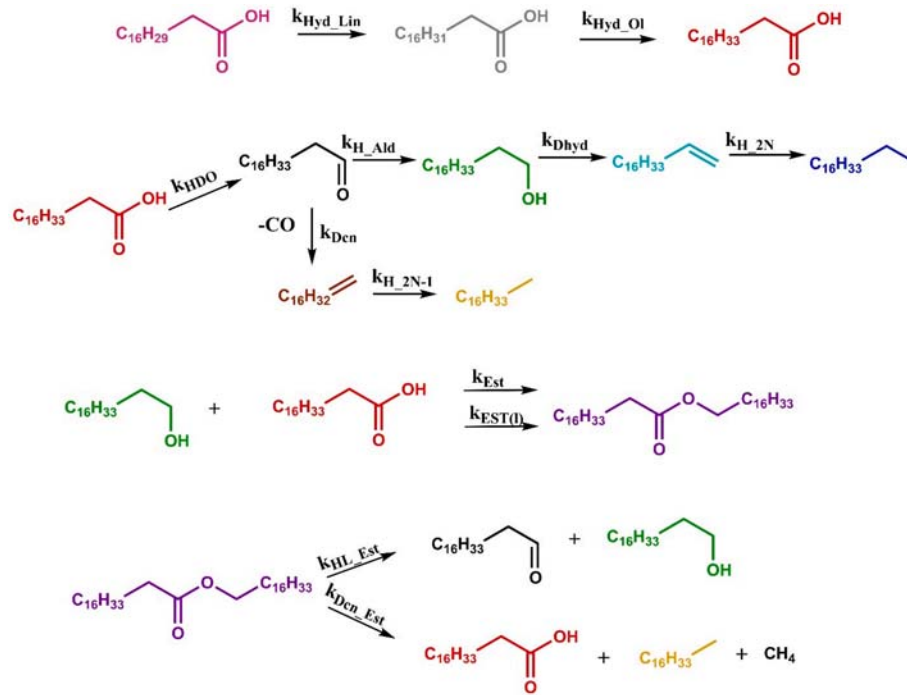
Fig. 1. The set of reactions used to describe the reactions.

which was sufficient due to the size of the supercell. The system was allowed to relax until the atomic forces dropped below 0.05 eV/Å. Several active sites and adsorption configurations were tested (e.g. hollow, top and bridge), where the thermodynamically most favorable is reported (see Fig. 5). The adsorption energies were calculated as:

$$E_{ads} = E_{species+surface} - E_{surface} - E_{species} \qquad (2)$$

where $E_{species+surface}$ is the total energy of the system, $E_{surface}$ is the energy of the empty surface slab and $E_{species}$ is the energy of studied molecule in vacuum.

Due to the size of the studied adsorbents, we modelled several shorter chains, did a linear regression on the acquired data set and extrapolated the energies to obtain the energy of the targeted species. Solvation effects were considered, but were ultimately not included following approaches by other authors [24,29] and due to extensive computational cost.

2.6. Kinetic modelling

Gas-Liquid mass transfer was previously described in the article [20]. Briefly the mass transfer coefficient (kL) of 1.29×10^{-5} was used with the mass transfer area of 0.0029 m². The kL was determined using the dead-end batch reactor results [30].

The included mass balances to describe the solid and liquid phase can be found in equations 3–6.

$$\frac{dC_{H_2,L}}{dt} = -k_{H_2ads} \times C_{H_2,L} \times C_{cat} + k_{H_2des} \times C_{H_2,S}$$

$$\times C_{cat} + \frac{k_L \times a \times \left(\frac{p}{He} \times \frac{M_{DD}}{\rho_{DD}} - C_{H_2L} \right)}{V_L} \qquad (3)$$

$$\frac{dC_{i,L}}{dt} = -k_{ads} \times C_{i,L} \times \frac{C_{FreeAS}}{C_{AS}} + k_{des} \times \frac{C_{i,S}}{V_L} \qquad (4)$$

$$\frac{dC_{H_2,S}}{dt} = k_{H_2ads} \times C_{H_2,L} - k_{H_2des} \times C_{H_2,S} \pm r_i \qquad (5)$$

$$\frac{dC_{i,S}}{dt} = k_{ads} \times C_{i,L} \times V_L \times \frac{C_{FreeAS}}{C_{AS}} - k_{des} \times C_{i,S} \pm r_i \qquad (6)$$

Liquid-solid mass transfer was described using adsorption and desorption functions. Adsorption was considered equivalent only dependent on the liquid phase concentration with adsorption parameter being fitted in a way for the adsorption being significantly faster than reaction rates. The initial guess was considered in a way that enabled fast hydrogenation reactions while enabling the existence of alkenes (which have strong adsorption energies) in the liquid phase.

$$r_{i,ads} = k_{ads} \times C_{i,L} \times \frac{C_{FreeAS}}{C_{AS}} \qquad (7)$$

Desorption was considered with DFT estimated energy barriers and described in the following form. The expression was taken from the work of Skubic et. al. [31] and modified with correction factor K to describe the process of desorption.

$$r_{i,des} = \frac{k_B T}{h} \times e^{\frac{Ead_i \times 96491}{KRT}} \qquad (8)$$

All reaction rates would take on of the following forms:

$$r_i = k_i \times C_{i,S} \times C_{H_2,S} \qquad (9)$$

$$r_i = k_i \times C_{i,S} \qquad (10)$$

$$r_i = k_i \times C_{i,S} \times C_{j,S} \qquad (11)$$

The temperature dependence of the reaction rate was described with Arrhenius equation.

$$k(T) = k(523K) \times e^{\frac{-Ea}{R}\left(\frac{1}{T} - \frac{1}{523} \right)} \qquad (12)$$

For the fitting of the shorter fatty acids – decanoic and myristic acid the kinetic expression from C_{18} acids were adapted with equations (13). The index j defines the specific x and E for C_{10} and C_{14}.

Table 1
Textural properties and composition of NiMo catalyst.

Catalyst	NiMo/Al$_2$O$_3$
Active phase	NiMoS$_x$
Deoxygenation active sites (μmol/m^{-2}(−|-))	0.3
BET Surface area (m^2/g)	170
Pore volume (cm^3 g^{-1})	0.471
Pore size (nm)	8.9
Total acidity (mmol/g)	1.22
Strong acidity (235 °C, mmol/g)	0.45
Medium acidity (150 °C, mmol/g)	0.31
Weak acidity (63 and 95 °C, mmol/g)	0.46

$$k_{i,j}(T) = x_j \times k_{i,C18}(523K) \times e^{\frac{-E_jEa}{R}\left(\frac{1}{T}-\frac{1}{523}\right)} \tag{13}$$

The following assumptions were followed when producing the model:

−The fatty acids were considered to desorb instantly upon hydrogenation of the double bonds due to very low alkane adsorption energy, to avoid a higher number of adsorption configurations. The assumption is supported by the hydrogenation being exothermic which enables instant desorption.[32].

−The hydrodeoxygenation of unsaturated fatty acids was neglected.

−The H$_2$O and CO transfer to gas-phase was neglected. Which was considered reasonable since they do not participate as reactants for the formation of products.

−The fatty alcohol dehydration and fatty aldehyde decarbonylation would yield liquid alkene products. This is in accordance with the literature on mechanisms of dehydration while the literature reports the formation of both adsorbed and desorbed alkene for decarbonylation, however, considering the similarities in isomer distribution and concentration of C$_{2N}$ and C$_{2N-1}$ alkene isomers in the liquid phase, and a very high adsorption barrier of alkene species it seems unlikely that hydrogenation of formed alkene is possible prior to desorption.

−All possible sorts of C-C scissions are grouped into hydrodeoxygenation – decarbonylation mechanism, the literature however discusses, the decarboxylation [20,33], or direct decarbonylation from fatty acids to alkanes without the desorption of intermediates [34]. We found that for the purpose of modelling a high variety between the values of decarbonylation and decarboxylation can be observed, while no reaction mechanism independent of hydrogen was observed, and thus only a single mechanism was chosen to describe the process.

The list of reactions with mass balances used in the model can be found in Table 2.

The results were modelled using MATLAB R2021b version. The weighted objective function was minimized using the combination of Nedler-Mead and Levenberg-Marquardt algorithms. The 95 % confidence intervals were calculated using "trust-region-reflective" algorithm.

$$f(k_n, Ea_n) = \sum_{j=1}^{EXP}\sum_{i=1}^{nS}\sum_{C=1}^{nC}(C_{j,i}^{exp} - C_{j,i}^{mod})^2 \tag{14}$$

3. Results and discussion

The reaction scheme is presented here for the better understanding and easier interpretation of the results is presented in Fig. 1. The colour scheme is the same in the modelling results. In Fig. 1 the first line represents the hydrogenation of unsaturated fatty acids, the second line represents the hydrodeoxygenation path of fatty acids, while the third and the fourth line represent the formation and hydrogenolysis of wax esters.

3.1. Catalyst characterization

In addition to the analysis provided in Table 1., the XRD and STEM analyses were conducted to describe the catalyst structure and

Table 2
Reactants and products based on the model.

Reactants	Products	Name of the reaction
C$_{18}$H$_{32}$O$_2$(s) + H$_2$(s)	C$_{18}$H$_{34}$O$_2$(l)	Hydrogenation of linoleic acid
C$_{18}$H$_{34}$O$_2$(s) + H$_2$(s)	C$_{18}$H$_{36}$O$_2$(l)	Hydrogenation of oleic acid
C$_{18}$H$_{36}$O$_2$(s) + H$_2$(s)	C$_{18}$H$_{36}$O(s) + H$_2$O(s)	Hydrodeoxygenation of saturated fatty acid
C$_{18}$H$_{36}$O(s) + H$_2$(s)	C$_{18}$H$_{38}$O(s)	Hydrogenation of fatty aldehyde
C$_{18}$H$_{36}$O(s)	C$_{17}$H$_{34}$(l) + H$_2$(s) + CO(s)	Decarbonylation
C$_{18}$H$_{38}$O(s)	C$_{18}$H$_{36}$(l) + H$_2$O(s)	Dehydration
C$_{18}$H$_{38}$O(s) + C$_{18}$H$_{36}$O$_2$(s)	C$_{36}$H$_{72}$O$_2$(s) + H$_2$O(s)	Esterification
C$_{36}$H$_{72}$O$_2$(s) + H$_2$(s)	C$_{18}$H$_{36}$O(s) + C$_{18}$H$_{38}$O(s)	Hydrogenolysis of esters
C$_{36}$H$_{72}$O$_2$(s) + H$_2$(s)	C$_{18}$H$_{36}$O$_2$(s) + C$_{17}$H$_{36}$(s) + CH$_4$(s)	Hydrogenolysis of esters via decarbonylation mechanism
C$_{18}$H$_{36}$ + H$_2$(s)	C$_{18}$H$_{38}$(s)	Hydrogenation of 2n alkenes
C$_{17}$H$_{34}$ + H$_2$(s)	C$_{17}$H$_{36}$(s)	Hydrogenation of 2n-1 alkenes
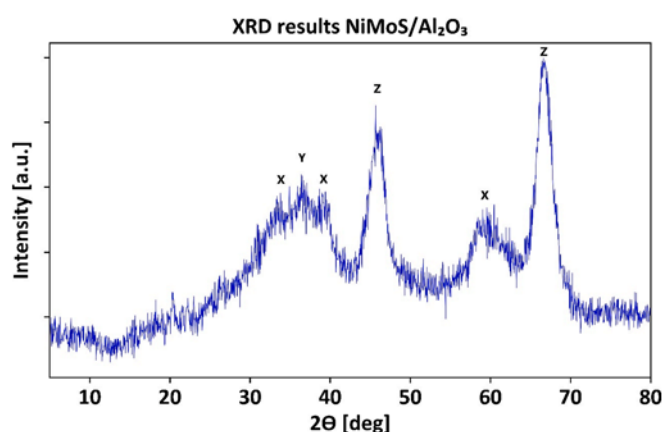
Fig. 2. XRD diffractogram of the investigated catalyst. MoS$_2$ – X, NiO – Y, γ-Al$_2$O$_3$ – Z.

composition Table 2.

The XRD graph (Fig. 2) shows the peaks of two phases of active metals – NiO which is expected to reduce at the reaction conditions to Ni^0 and MoS$_x$. The results show a highly amorphous active metal phase which, according to the literature, is beneficial to catalytic activity of sulfided catalysts [35]. The results are in accordance with results by del Rio et. al. [36].

The XRD data was corroborated with STEM-EDS elemental analysis (Fig. 3). The data shows that molybdenum and sulphur are almost always located in the same areas of the sample which indicates high degree of sulfidation of Mo sites. Sulphur covers 99.55 % of the molybdenum sites and Mo overlaps with 98,67 % of S sites. Meanwhile up to 52,05 % of the nickel is bound together in the nickel promoted sulphur-molybdenum complex which was considered the main active site for hydrodeoxygenation reactions. Some smaller amount, i.e. 0,55 % of nickel is bonded with sulphur forming NiS and 0,15 % is bonded with molybdenum in NiMo without the presence of sulphur peak. The rest of present nickel, i.e. 47,25 % of peaks is found to be separate and located on the surface of the support. This indicates that NiS species that can be found in literature [34] are likely not present in high amounts in the investigated catalyst possibly due to storage under air atmosphere or due to impact of sulfidation conditions [37,38].

The overlap of peaks between elements depends on density of atoms which are bonded to the support. If the concentration of peaks is high, the overlaps of peaks are higher as well. The exception is the overlap
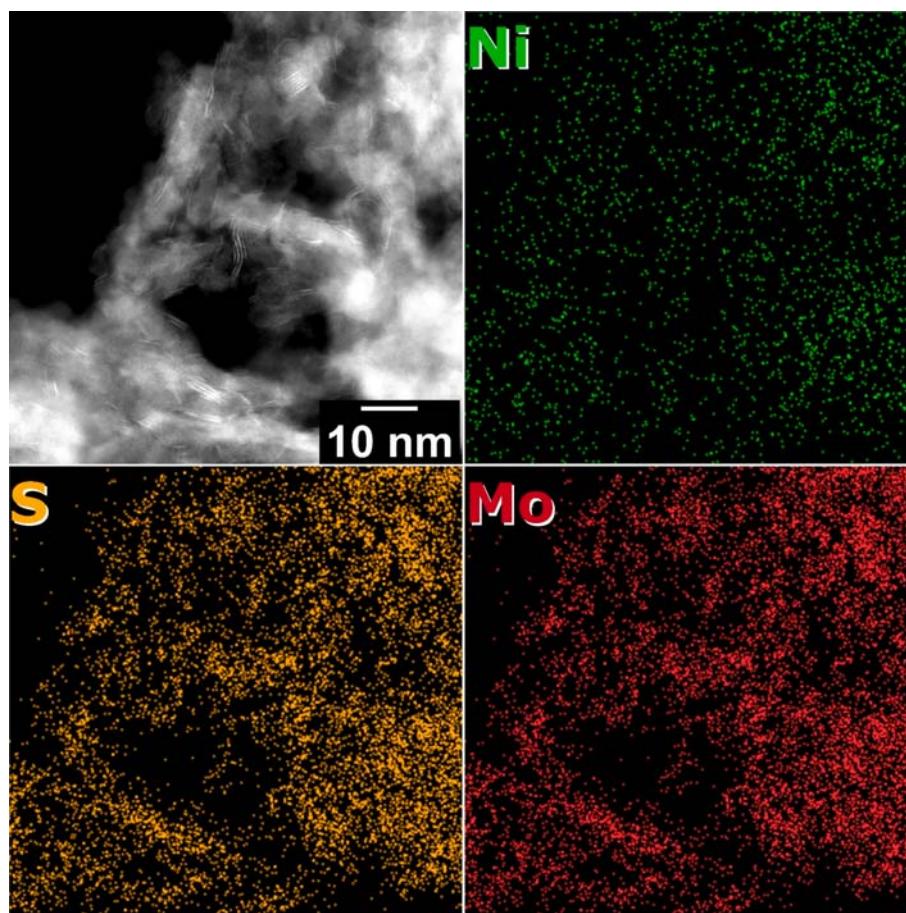
Fig. 3. STEM micrograph with corresponding elemental distribution maps for Ni (green), S (yellow), and Mo (red).
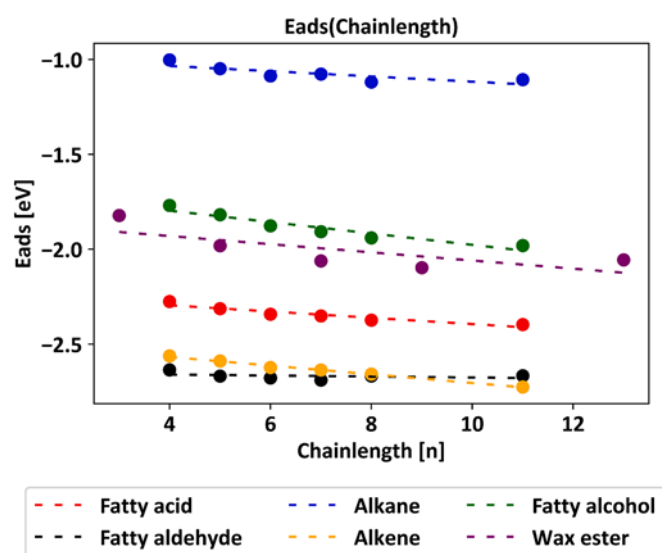

Fig. 4. The interpolation lines of the obtained energies for acids, alkenes, and alkanes.

between Mo and S which is always consistent, at around 99 %. Since the results are much dependent on the density of EDS spectrum responses, we have decided to use the Monte Carlo statistic method to compare the observed coverage with random coverage, it turns out that the Monte Carlo prediction was within the 10 % the observed coverage regardless of density of peaks for Ni-Mo and Ni-S peak overlaps and which indicates

that the Ni promotion of Mo at chosen sulfidation conditions is likely a random event based on the presence of both species on the surface limited by kinetics of mass transport. Ni and Mo are deposited in proximity as small amorphous particles, which according to literature [39,40], complement each other via Ni MoS_x promotion. To conclude, both the STEM and XRD results confirm that the Mo is in sulphide form, while some Ni is present in metallic form to which it is reduced during the heat-up period. The literature reports that the lack of NiS could be a consequence of $NiMoS/Al_2O_3$ catalyst storage [37].

3.2. DFT calculations (adsorptions)

The surface slab was probed by adsorption configurations, where the thermodynamically most stable ones are reported. As mentioned in the computational details, we obtained the adsorption energies of longer chains species by extrapolating the energies obtained from several shorter chain molecules. As evident from Fig. 4, the adsorption energy linearly increases because it also depends on dispersion interactions, which monotonically increase with chain length. The interpolation lines are also highly dependent on the interacting functional group. Fig. 4 shows alkanes weakly interact with the surface, thus the y intercept is

Table 3
The extrapolated adsorption energies for linear hydrocarbons with different functional groups.

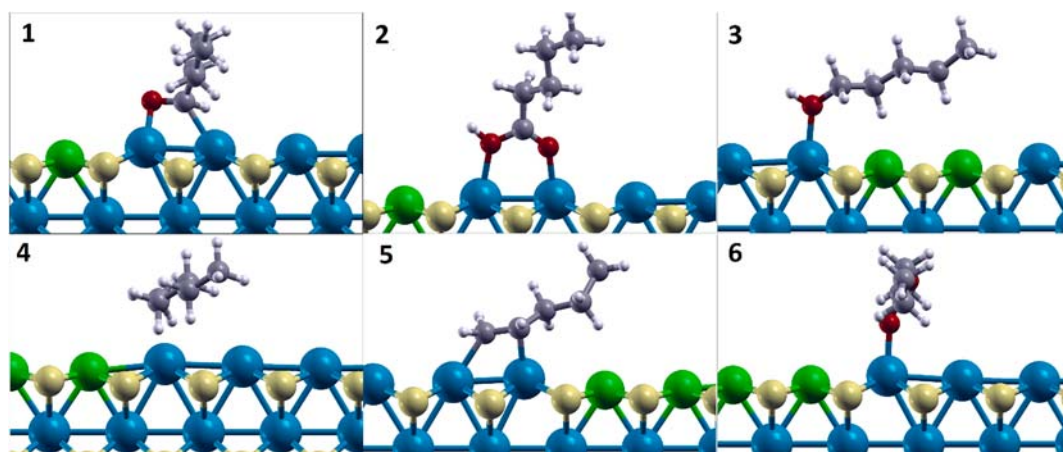| Ead [eV]	Acids	Aldehydes	Alcohols	Alkanes	Alkenes	Esters
C_{10}	−2.39	−2.68	−1.98	−1.12	−2.70	−2.06
C_{14}	−2.46	−2.69	−2.10	−1.17	−2.80	−2.14
C_{18}	−2.53	−2.70	−2.22	−1.23	−2.89	−2.23

Fig. 5. Adsorption configurations for pentanal (1), pentanoic acid (2), pentanol (3), pentane (4), pentene (5) and Ester (6). Color code; green-Ni, blue-Mo, yellow-S, white-H, red-O and grey-C.

Table 4
The kinetic and adsorption results of the modelling with 95 % confidence intervals.

index	reaction rate constants C18 [min^{-1} g$_{cat}$ mol^{-1}]	95 % confidence interval [%]	Ea	95 % confidence interval [%]
Hyd_Lin	2.5×10^5	>100	14	27
Hyd_Ol	2.6×10^6	>100	27	53
HDO	9.2×10^3	8	143	5
H_Ald	7.3×10^4	47	108	14
Dcn	4.6 [a]	36	161	7
Dhyd	59 [a]	10	65	11
Est	6×10^{5b}	>100	78	>100
hlest	2.2×10^4	>100	124	>100
Dcn_Est	7.5×10^1	66	57	>100
H_2N	2.8×10^3	11	60	20
H_2N-1	1.8×10^3	23	72	19
Est(l)	2.2×10^{-2c}	23	29	8
Decanoic and Myristic acid				
i	x$_i$		E$_i$	
C$_{10}$	2.17		0.69	
C$_{14}$	1.69		0.73	

Adsorption parameters			
Parameter	Value	Unit	
k_ads	10^3	min^{-1}	
K	2.1	/	
k$_{H2ads}$	12.59	min^{-1} g$_{cat}^{-1}$ L	
k$_{H2ads}$ /k$_{H2des}$	8×10^{-4}	min^{-1} g$_{cat}^{-1}$ L	

For [a],[b] and [c] the units change to min^{-1}, min^{-1}mol^{-1} and min^{-1}mol^{-1}L respectively.

estimated at -0.98, whereas for a strongly interacting system e.g. fatty aldehyde the y intercept is at -2.65 (see Figure S2 in the Supplementary).

The results in Table 3 show why aldehydes are often negligible in concentration, due to their high desorption barriers resulting in relatively high coverage and high reactivity they are rapidly transformed to intermediates with lower binding energies. Importantly, alcohols and esters have lower desorption energies which agree with experimental observations in the literature [20,33] These results also explain why the adsorption of alkanes can be neglected and that both the solvent and the products have negligible coverages of the catalyst at all concentrations. The double bonds adsorb very strongly on the catalyst which explains the observed hydrogenation – hydrodeoxygenation order and low observed alkenes concentrations.

Fig. 5 shows the considered adsorption configurations for all functionalities present in the model. Additionally, the adsorption energies for water $- -1.22$ eV and for CO $- -2.08$ eV were used in the model.

3.3. Kinetic results

The mechanisms used can be seen on Fig. 1. They include typical hydrodeoxygenation with aldehyde decarbonylation and hydrogenation to fatty alcohols. The fatty alcohols dehydration and decarbonylation of fatty aldehydes for the respective C$_{2N}$ and C$_{2N-1}$ alkenes. The alkenes can be hydrogenated to alkanes. Kinetic results are presented in Table 4. The H$_2$ concentration on the catalyst was calculated based on experimental pressure via Eq. (3) and (5) however, for the catalyst performance comparison the concentration of 3×10^{-4} mol g$_{cat}^{-1}$ can be used.
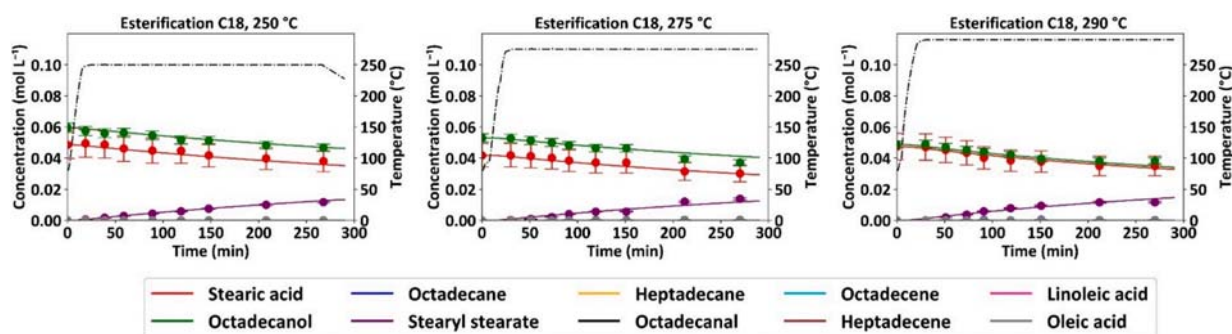

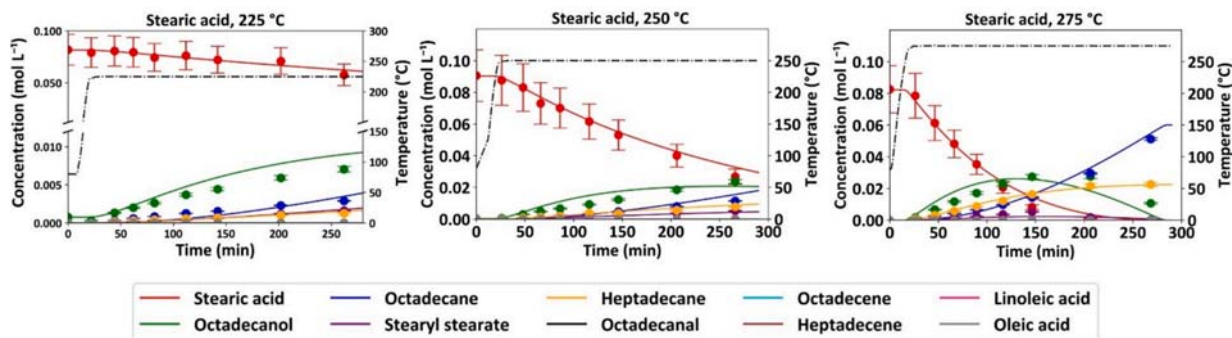**Fig. 6.** The rate of homogeneous esterification at 250, 275 and 290 °C.

Fig. 7. The concentration profiles and model fits for stearic acid HDO at different temperatures.
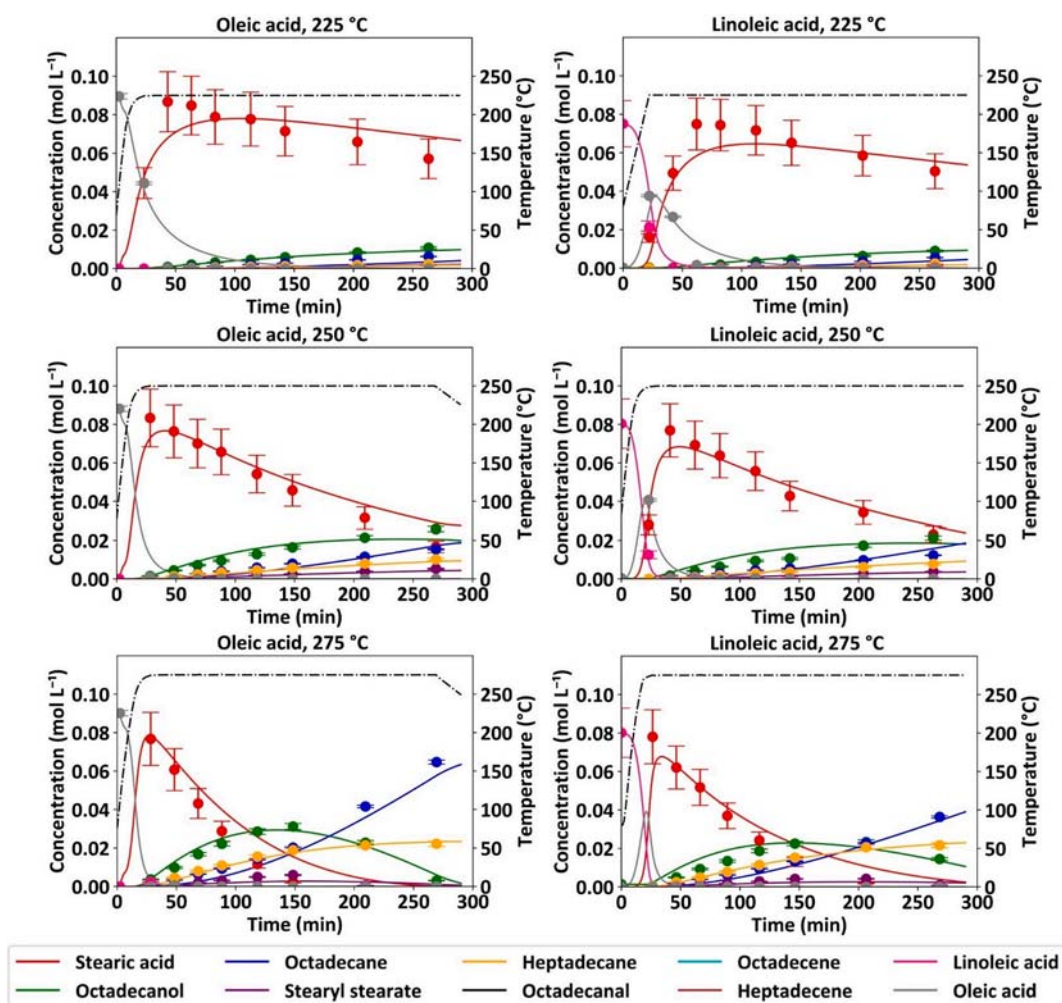

Fig. 8. The concentration profiles for experiments with oleic and linoleic acid.

3.4. The homogeneous reactions

The literature mostly neglects the homogeneous reactions since they cannot be observed with only a single compound however the fatty acid and fatty alcohol clearly react in the dodecane solution in the observed temperature range (Fig. 6). However, the reverse reaction – hydrolysis of palmityl palmitate was negligible. The reaction should be even more prevalent at higher concentrations since we only used ∼ 1.25 wt% mixture of each reactant while the reaction rate scales with the square of concentration unlike catalytic reactions which are capped with the number of active sites. Based on these facts, some results in the

literature, especially of fatty alcohols synthesis, should be critically considered, and perhaps re-examined.

3.5. The heterogeneous reactions

The stearic acid fits with determined desorption energy barriers are comparable to literature with the rates and the activation barriers being similar, low activation energies for hydrogenations and relatively high – about 100 kJ for deoxygenation reactions [15,33,34,41]. The first step of hydrogenolysis of the stearic acid might be a bit of an outlier from the literature, because the hydrogenolysis and direct decarboxylation are
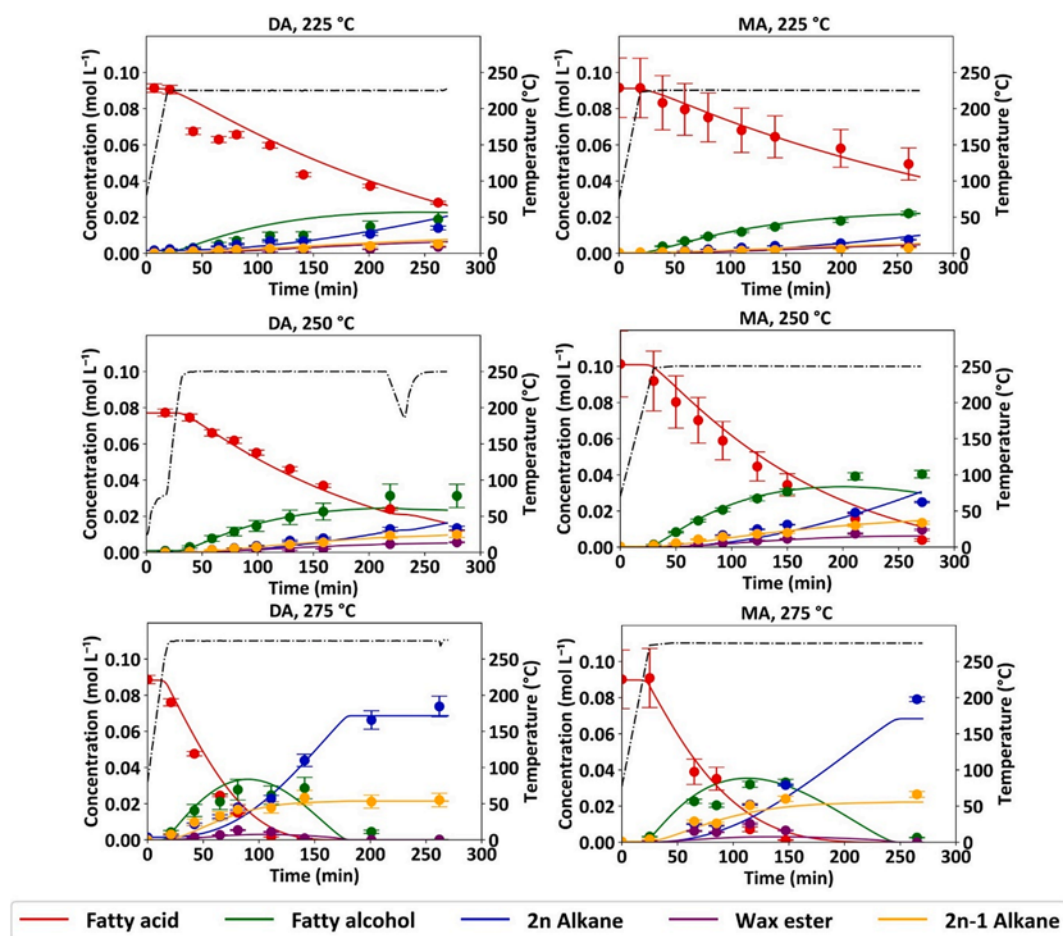
Fig. 9. Experimental and modelling results for different fatty acid chain lengths at different temperatures.

usually separated. However, due to a very high hydrogenolysis to decarboxylation ratio the direct decarboxylation was neglected here. The model describes the overall trends – concentration increase and decrease time periods well (Fig. 7, Figure S1); however, the already standard "bellies" appear on the fatty alcohol concentration profiles. This is likely due to either direct transformation from fatty aldehyde directly to alkane or alkene or the fatty alcohol being able to access more active sites than fatty acids due to its more linear nature. Regardless these discrepancies could be corrected by the consideration of the direct transformation, however, we have decided against it since the purpose of the model was to illustrate that the adsorption barriers can be implemented directly into current models to improve the understanding and explain the observed concentrations and the integration of such parallel reactions would simplify the fitting significantly but would require a significant increase in the number of experiments for the results to be meaningful. The calculated adsorption energies also explain why the aldehydes are seldom detected, with their high adsorption energies and high reactivity the concentrations can often be at the edge of GC–MS detection limit.

3.6. The impact of saturation

All the C_{18} reactions were fit with the same reaction constants which clearly shows some discrepancies in the reaction rates (Fig. 8, Figure S1). Unsaturated acids, oleic and linoleic acid, would convert faster than stearic acid which is notable with most of stearic experimental data being positioned below the predicted line unlike in stearic acid where they fit nearly perfectly. The literature reports very high dependence between saturation and catalyst stability and recommends

pre-hydrogenation steps of unsaturated oils [42,43]. We have not found the deactivation mechanisms to impact our results likely due to batch setup, low initial concentrations, and relatively mild conditions. However, results previously observed in the literature can be explained by the very high adsorption energy of double bonds which is the cause of coking due to unsaturated fatty acids being very likely to adsorb via double bonds rather than via oxygen head and in that way bind the double bonds together via Diels-Alder reaction. We also show that the adsorption energies increase via chain length increase such products are then a lot less likely to desorb and would result in catalyst coking [44].

3.7. The impact of fatty acid length

In the literature it is possible to find the catalytic results for different model compounds and beyond that, different oils can be used for the preparation of renewable fuels however the impact fatty acid chain length is usually neglected and mostly assumed negligent. Thus, we have compared different length fatty acids, namely decanoic acid (C_{10}) and myristic acid (C_{14}) to observe and describe the differences in the kinetics. We found that the selectivity between the C_{2N} and C_{2N-1} alkanes remains the same at around 75 % of C_{2N} for 275 It would decrease with temperature increase and increase with pressure increase. The concentration change would impact it by formation of more wax esters in liquid phase which would increase selectivity for C_{2N} products. All kinetic parameters and activation energies change with the similar trend. Comparing Fig. 9 with Figs. 7 and 8 it can be observed the decanoic acid at 275 °C is consumed about 60 min earlier than the stearic acid at the same initial concentration. The results show that kinetic constants are impacted significantly increasing the rate of the reactions at the same
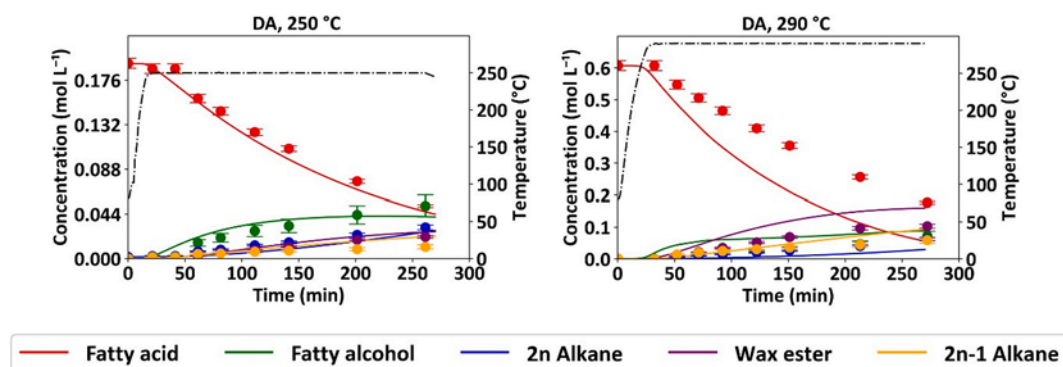
Fig. 10. Validation of the model for different initial concentrations of decanoic acid.

temperature, however the energies of activation are lowered significantly as well thus the reaction rate might be similar at very high reaction temperatures where the reaction barriers become less relevant.

3.8. Validation via intensification

We have done the intensification of the process to confirm the correctness of the approach, Fig. 10 shows the results of the 2-times and the 6-times higher initial concentration at 250 and 290 °C respectively. While the 2-times concentration shows a great fit. The 6-times concentration shows some deviation, likely for several reasons, the concentrations here were normalized due to higher deviation, the fatty acid might undergo direct HDO to alkanes/alkenes without forming fatty alcohol intermediate, similar mechanisms were observed in our other unrelated works with NiMoS$_x$/γ-Al$_2$O$_3$ catalyst, as consequence the fatty alcohol, formation should be slower, which in parallel should also lower the amount of predicted wax esters and lower homogeneous fatty acid conversion. Additionally, the wax ester formation and the reaction rate might thus increase less than observed for the catalytic transformations. Thus, for works in the future we suggest using shorter chain model compounds per example decanoic acid, which are, due to their low melting point, significantly easier to work with in laboratory experimental settings at higher concentrations and then based on those results extrapolation to longer chain fatty acids. Regardless, considering the scope of the experimental data the model shows good predictions even outside of the fitted concentration and temperature intervals and would require a minimal adaptation to describe a very wide interval of experimental conditions.

4. Conclusion

Through this work we have stepped a bit closer to the goal of describing the intrinsic rates via the number of catalytic sites rather than by fitting of several parameters. We show that the extrapolated adsorption energies can be derived from first principles even for molecules that are computationally demanding and can be used instead of fitted Langmuir adsorption equilibrium constant. The adsorption energy can thus very well explain the observed events such as very fast hydrogenation of double bonds, very low aldehyde concentration, fatty acid "poisoning" the sites for fatty alcohol dehydration and ester hydrogenolysis. While a minor correction is needed in the form of the correction factor, the equation for the first principles desorption can be utilized. Beyond that we show that both the kinetic and adsorption barriers follow same trend of increasing with chain length. It means that the longer molecules will react slower and cover more of the catalytic sites than the shorter counterparts. We also show that most of the esterification in the NiMoS$_x$ system is the homogeneous reaction and thus should never be discarded for modelling of preparation of renewable fuels or fatty alcohols as it scales linearly with both fatty alcohol and fatty acid concentration.

CRediT authorship contribution statement

Matej Žula: Writing – review & editing, Writing – original draft, Visualization, Validation, Software, Methodology, Investigation, Formal analysis, Data curation, Conceptualization. **Žan Kovačič:** Writing – original draft, Methodology, Formal analysis, Data curation, Conceptualization. **Vid Bačar:** Investigation, Formal analysis, Data curation. **Michal Mazur:** Writing – review & editing, Writing – original draft, Visualization, Methodology, Investigation, Funding acquisition, Formal analysis, Conceptualization. **Matej Huš:** Writing – review & editing, Writing – original draft, Visualization, Validation, Software, Methodology, Investigation, Formal analysis, Data curation, Conceptualization. **Blaž Likozar:** Writing – review & editing, Supervision, Project administration, Funding acquisition.

Declaration of competing interest

The authors declare that they have no known competing financial interests or personal relationships that could have appeared to influence the work reported in this paper.

Data availability

Data will be made available on request.

Appendix A. Supplementary data

Supplementary data to this article can be found online at https://doi.org/10.1016/j.cej.2024.156348.

References

[1] S.S. Bello, C. Wang, M. Zhang, H. Gao, Z. Han, L. Shi, F. Su, G. Xu, A Review on the Reaction Mechanism of Hydrodesulfurization and Hydrodenitrogenation in Heavy Oil Upgrading, Energy Fuel 35 (2021) 10998–11016, https://doi.org/10.1021/acs.energyfuels.1c01015.

[2] T. Stedile, L. Ender, H.F. Meier, E.L. Simionatto, V.R. Wiggers, Comparison between physical properties and chemical composition of bio-oils derived from lignocellulose and triglyceride sources, Renew. Sustain. Energy Rev. 50 (2015) 92–108, https://doi.org/10.1016/j.rser.2015.04.080.

[3] D. Bouzouita, A. Lelevic, C. Lorentz, R. Venderbosch, T.H. Pedersen, C. Geantet, Y. Schuurman, Co-processing bio-liquids with vacuum gasoil through

hydrocracking, Appl Catal B 304 (2022), https://doi.org/10.1016/j.apcatb.2021.120911.

[4] C. Zhu, O.Y. Gutiérrez, D.M. Santosa, M. Flake, R. Weindl, I. Kutnyakov, H. Shi, H. Wang, Kinetics of nitrogen-, oxygen- and sulfur-containing compounds hydrotreating during co-processing of bio-crude with petroleum stream, Appl Catal B 307 (2022), https://doi.org/10.1016/j.apcatb.2022.121197.

[5] P. Arora, H. Ojagh, J. Woo, E. Lind Grennfelt, L. Olsson, D. Creaser, Investigating the effect of Fe as a poison for catalytic HDO over sulfided NiMo alumina catalysts, Appl Catal B (2018) 240–251, https://doi.org/10.1016/j.apcatb.2018.01.027.

[6] P. Arora, H. Abdolahi, Y.W. Cheah, M.A. Salam, E.L. Grennfelt, H. Rådberg, D. Creaser, L. Olsson, The role of catalyst poisons during hydrodeoxygenation of renewable oils, Catal Today (2020), https://doi.org/10.1016/j.cattod.2020.10.026.

[7] M.A. Salam, D. Creaser, P. Arora, S. Tamm, E.L. Grennfelt, L. Olsson, Influence of bio-oil phospholipid on the hydrodeoxygenation activity of NiMoS/Al2O3 catalyst, Catalysts 8 (2018), https://doi.org/10.3390/catal8100418.

[8] O. Hinr, / Chsen, E. Rosowski, M. Muhler, G. Ertl, THE MICROKINETICS OF AMMONIA SYNTHESIS CATALYZED BY CESIUM-PROMOTED SUPPORTED RUTHENIUM, 1996.

[9] M.S. Frei, M. Capdevila-Cortada, R. García-Muelas, C. Mondelli, N. López, J. A. Stewart, D. Curulla Ferré, J. Pérez-Ramírez, Mechanism and microkinetics of methanol synthesis via CO2 hydrogenation on indium oxide, J Catal 361 (2018) 313–321, https://doi.org/10.1016/j.jcat.2018.03.014.

[10] L. Xiao, F. Ma, Y.A. Zhu, Z.J. Sui, J.H. Zhou, X.G. Zhou, D. Chen, W.K. Yuan, Improved selectivity and coke resistance of core-shell alloy catalysts for propane dehydrogenation from first principles and microkinetic analysis, Chem. Eng. J. 377 (2019), https://doi.org/10.1016/j.cej.2018.09.210.

[11] X. Cao, S. Wu, J. Zhao, F. Long, S. Jia, X. Zhang, J. Xu, J. Jiang, Synthesis of novel Mo-Ni@Al2O3 catalyst for converting fatty acid esters into diesel-range alkanes with enhanced hydrodeoxygenation selectivity, Appl Catal B 343 (2024), https://doi.org/10.1016/j.apcatb.2023.123506.

[12] D. Liu, Z. Li, C.C. Wu, L. Song, P.P. Wu, M. Li, C. Wang, Z. Men, Z. Yan, I.D. Gates, Exploration of in-situ formed MoSx catalyst for co-hydrodeoxygenation of sawdust and vacuum gas oil in pilot-scale plant, Appl Catal B 297 (2021), https://doi.org/10.1016/j.apcatb.2021.120499.

[13] A.V. Vutolkina, I.G. Baigildin, A.P. Glotov, A.A. Pimerzin, A.V. Akopyan, A. L. Maximov, E.A. Karakhanov, Hydrodeoxygenation of guaiacol via in situ H2 generated through a water gas shift reaction over dispersed NiMoS catalysts from oil-soluble precursors: Tuning the selectivity towards cyclohexene, Appl Catal B 312 (2022), https://doi.org/10.1016/j.apcatb.2022.121403.

[14] D. Ryaboshapka, L. Piccolo, M. Aouine, P. Bargiela, V. Briois, P. Afanasiev, Ultradispersed (Co)Mo catalysts with high hydrodesulfurization activity, Appl Catal B 302 (2022), https://doi.org/10.1016/j.apcatb.2021.120831.

[15] J.L. Castagnari Willimann Pimenta, M. de Oliveira Camargo, R. Belo Duarte, O.A. Andreo dos Santos, L.M. de Matos Jorge, A novel kinetic model applied to heterogeneous fatty acid deoxygenation, Chem Eng Sci 230 (2021). https://doi.org/10.1016/j.ces.2020.116192.

[16] P. Agarwal, N. Evenepoel, S.S. Al-khattat, M.T. Klein, Molecular-Level Kinetic Modeling of Methyl Laurate: the Intrinsic Kinetics of Triglyceride Hydroprocessing (2018), https://doi.org/10.1021/acs.energyfuels.8b00647.

[17] S. Reddy Yenumala, S.K. Maity, D. Shee, Reaction mechanism and kinetic modeling for the hydrodeoxygenation of triglycerides over alumina supported nickel catalyst, Reaction Kinetics, Mechanisms and Catalysis 120 (2017) 109–128, https://doi.org/10.1007/s11144-016-1098.

[18] X. Liu, M. Yang, Z. Deng, A. Dasgupta, Y. Guo, Hydrothermal hydrodeoxygenation of palmitic acid over Pt/C catalyst: Mechanism and kinetic modeling, Chem. Eng. J. 407 (2021) 126332, https://doi.org/10.1016/j.cej.2020.126332.

[19] Y. Bie, J. Lehtonen, J. Kanervo, Hydrodeoxygenation (HDO) of methyl palmitate over bifunctional Rh/ZrO2 catalyst: Insights into reaction mechanism via kinetic modeling, Appl Catal A Gen 526 (2016) 183–190, https://doi.org/10.1016/j.apcata.2016.08.030.

[20] M. Žula, M. Grilc, B. Likozar, Mechanistic reaction micro-kinetics-based structure–activity relationships for palmitic acid hydrodeoxygenation over NiMoSx/Al2O3 catalysts, Chem. Eng. J. 467 (2023), https://doi.org/10.1016/j.cej.2023.143425.

[21] M. Grilc, B. Likozar, Levulinic acid hydrodeoxygenation, decarboxylation and oligomerization over NiMo/Al2O3 catalyst to bio-based value-added chemicals: Modelling of mass transfer, thermodynamics and micro-kinetics, Chem. Eng. J. 330 (2017) 383–397, https://doi.org/10.1016/j.cej.2017.07.145.

[22] J.J. Mortensen, L.B. Hansen, K.W. Jacobsen, Real-space grid implementation of the projector augmented wave method, Phys Rev B Condens Matter Mater Phys 71 (2005) 1–11, https://doi.org/10.1103/PhysRevB.71.035109.

[23] S. Grimme, A. Hansen, J.G. Brandenburg, C. Bannwarth, Dispersion-Corrected Mean-Field Electronic Structure Methods, Chem Rev 116 (2016) 5105–5154, https://doi.org/10.1021/acs.chemrev.5b00533.

[24] M. Ruinart De Brimont, C. Dupont, A. Daudin, C. Geantet, P. Raybaud, Deoxygenation mechanisms on Ni-promoted MoS 2 bulk catalysts: A combined experimental and theoretical study, J Catal 286 (2012) 153–164, https://doi.org/10.1016/j.jcat.2011.10.022.

[25] E. Krebs, B. Silvi, A. Daudin, P. Raybaud, A DFT study of the origin of the HDS/HydO selectivity on Co(Ni)MoS active phases, J Catal 260 (2008) 276–287, https://doi.org/10.1016/j.jcat.2008.09.026.

[26] M. Sun, A.E. Nelson, J. Adjaye, Adsorption and hydrogenation of pyridine and pyrrole on NiMoS: An ab initio density-functional theory study, J Catal 231 (2005) 223–231, https://doi.org/10.1016/j.jcat.2005.01.021.

[27] L. Bengtsson, Dipole correction for surface supercell calculations, Phys Rev B Condens Matter Mater Phys 59 (1999) 12301–12304, https://doi.org/10.1103/physrevb.61.16921.

[28] H.J. Monkhorst, J.D. Pack, Special points for Brillouin-zone integrations, Phys Rev B 13 (1976) 5188–5192, https://doi.org/10.1103/PhysRevB.16.1748.

[29] A. Travert, C. Dujardin, F. Maugé, E. Veilly, S. Cristol, J.F. Paul, E. Payen, CO adsorption on CoMo and NiMo sulfide catalysts: A combined IR and DFT study, J. Phys. Chem. B 110 (2006) 1261–1270, https://doi.org/10.1021/jp0536549.

[30] R. V Chaudhari, R. V Gholap, G. Emlg, H. Hofmann, Gas-Liquid Mass Transfer in ' ' Dead-End" Autoclave Reactors, n.d.

[31] L. Skubic, D. Kopač, B. Huš, Microkinetic modelling of heterogeneous catalysis revisited: Adsorption energies can triumph over activation barriers, Appl Surf Sci 601 (2022), https://doi.org/10.1016/j.apsusc.2022.154135.

[32] A.J. Dijkstra, Kinetics and mechanism of the hydrogenation process - the state of the art, Eur. J. Lipid Sci. Technol. 114 (2012) 985–998, https://doi.org/10.1002/ejlt.201100405.

[33] P. Arora, E.L. Grennfelt, L. Olsson, D. Creaser, Kinetic study of hydrodeoxygenation of stearic acid as model compound for renewable oils, Chem. Eng. J. 364 (2019) 376–389, https://doi.org/10.1016/j.cej.2019.01.134.

[34] M.F. Wagenhofer, E. Baráth, O.Y. Gutiérrez, J.A. Lercher, Carbon-Carbon Bond Scission Pathways in the Deoxygenation of Fatty Acids on Transition-Metal Sulfides, ACS Catal 7 (2017) 1068–1076, https://doi.org/10.1021/acscatal.6b02753.

[35] Y. Aray, J. Rodríguez, A.B. Vidal, S. Coll, Nature of the NiMoS catalyst edge sites: An atom in molecules theory and electrostatic potential studies, J Mol Catal A Chem 271 (2007) 105–116, https://doi.org/10.1016/j.molcata.2007.02.016.

[36] J.I. del Río, F. Cardeño, W. Pérez, J.D. Peña, L.A. Rios, Catalytic hydrotreating of jatropha oil into non-isomerized renewable diesel: Effect of catalyst type and process conditions, Chem. Eng. J. 352 (2018) 232–240, https://doi.org/10.1016/j.cej.2018.07.021.

[37] C.E. Scott, M.J. Perez-Zurita, L.A. Carbognani, H. Molero, G. Vitale, H.J. Guzmán, P. Pereira-Almao, Preparation of NiMoS nanoparticles for hydrotreating, Catal Today 250 (2015) 21–27, https://doi.org/10.1016/j.cattod.2014.07.033.

[38] P. Priecel, D. Kubička, L. Čapek, Z. Bastl, P. Ryśánek, The role of Ni species in the deoxygenation of rapeseed oil over NiMo-alumina catalysts, Appl Catal A Gen 397 (2011) 127–137, https://doi.org/10.1016/j.apcata.2011.02.022.

[39] L. Zhang, G. Karakas, U.S. Ozkan, NiMoS/γ-Al 2 O 3 Catalysts: The Nature and the Aging Behavior of Active Sites in HDN Reactions, 1998.

[40] M. Grilc, B. Likozar, J. Levec, Hydrodeoxygenation and hydrocracking of solvolysed lignocellulosic biomass by oxide, reduced and sulphide form of NiMo, Ni, Mo and Pd Catalysts, Appl Catal B 150–151 (2014) 275–287, https://doi.org/10.1016/j.apcatb.2013.12.030.

[41] B. Hočevar, M. Grilc, M. Huš, B. Likozar, Mechanism, ab initio calculations and microkinetics of straight-chain alcohol, ether, ester, aldehyde and carboxylic acid hydrodeoxygenation over Ni-Mo catalyst, Chem. Eng. J. 359 (2019) 1339–1351, https://doi.org/10.1016/j.cej.2018.11.045.

[42] J.I. del Río, W. Pérez, F. Cardeño, J. Marín, L.A. Rios, Pre-hydrogenation stage as a strategy to improve the continuous production of a diesel-like biofuel from palm oil, Renew, Energy 168 (2021) 505–515, https://doi.org/10.1016/j.renene.2020.12.086.

[43] T.H. Kim, K. Lee, M.Y. Kim, Y.K. Chang, M. Choi, Effects of Fatty Acid Compositions on Heavy Oligomer Formation and Catalyst Deactivation during Deoxygenation of Triglycerides, ACS Sustain Chem Eng 6 (2018) 17168–17177, https://doi.org/10.1021/acssuschemeng.8b04552.

[44] T. Ročnik Kozmelj, M. Žula, J. Teržan, B. Likozar, U. Maver, L. Činč Ćurić, E. Jasiukaitytė-Grojzdek, M. Grilc, Understanding stability, oligomerization and deactivation during catalytic lignin hydrodeoxygenation by mechanistic reaction micro-kinetics linked with 3D catalyst particle nanotomography, J Clean Prod 414 (2023), https://doi.org/10.1016/j.jclepro.2023.137701.